Shap. Mem. Superelasticity
https://doi.org/10.1007/s40830-024-00494-w

ORIGINAL RESEARCH ARTICLE

Advanced Material Thermomechanical Modelling of Shape Memory Alloys Applied to Automotive Design

M. Battaglia[1] · A. Sellitto[1] · A. Giamundo[2] · M. Visone[2] · A. Riccio[1]

Received: 30 March 2024 / Revised: 22 May 2024 / Accepted: 27 May 2024

Abstract This study introduces an innovative approach to enhancing aerodynamic efficiency in automotive applications by exploiting shape memory alloy technology. To this end, a thorough investigation of the thermomechanical behaviour of these alloys was conducted in the paper. Using a UMAT subroutine, the pseudoelastic effect and the shape memory effect of these smart materials were analysed numerically simultaneously, allowing accurate predictions of their behaviour under different loads, and facilitating the design and optimization of devices and systems based on SMAs. Therefore, the article proposes an innovative solution to optimize aerodynamic efficiency by using a Grille Shutter with variable openings. The Active Grille Shutter uses a bistable SMA actuator, allowing two optimal opening positions for specific load conditions. These actuators hold two stable states without energy consumption, ensuring efficient and reliable operation and allowing rapid transitions between the two states, making them ideal for applications that require timely responses. By using this specially designed and numerically analysed system, it has been confirmed that suitably dimensioned shape memory springs can guarantee a movement of the blades of the 90°, allowing an improvement in vehicle efficiency of about 4% at a speed of 140 km/h.

Keywords Adaptive aerodynamics · Morphing · Shape memory alloys · Actuators · FEM

✉ M. Battaglia
miriam.battaglia@unicampania.it

[1] Department of Engineering, University of Campania "Luigi Vanvitelli", via Roma 29, 81031 Aversa, CE, Italy

[2] BLUE Engineering, Via Ex Aeroporto 30/32, 80038 Pomigliano d'Arco, NA, Italy

Introduction

Over the past few years, there has been an increase in the development of new technologies to improve the aerodynamic performance of aircraft and vehicles. These technologies focus on using moving surfaces to change the curvature of the skin or modify the angle of attack of the entire profile [1–3]. Moving surfaces can be used to reduce drag, improve lift, and increase manoeuvrability. For example, variable-sweep wings [4] can be used to optimize the wing shape for different flight conditions, while active wingtips can be used to reduce drag and improve fuel efficiency. One of the most promising new technologies to improve aerodynamic performance is shape-changing surfaces [5]. These surfaces can be used to morph the shape of the aircraft or vehicle in real time, depending on the flight conditions [6, 7]. This can lead to significant reductions in drag and improvements in lift.

The investigation of aerodynamics is significant in the field of engineering, with relevance to the automotive sector. This discipline analyses and proposes targeted solutions to improve vehicle performance and efficiency. Initially oriented towards the analysis of automotive bodies with a simple profile [8], automotive aerodynamics has progressively adopted numerical implementation to examine component-specific details, focussing on problems and their solutions. Current analyses increasingly consider specific vehicle characteristics, allowing for targeted design interventions to provide benefits. For example, previous studies have shown that the inclusion of a spoiler and diffuser can lead to a maximum drag reduction of 16% on a race car [9]. Similar analyses also focus on the aerodynamic behaviour of SUVs, with and without spoilers [10] or propose design solutions to improve the fuel economy of buses [11]. In this context, adaptive aerodynamics represents

Published online: 24 June 2024

an innovative approach based on the ability to change the aerodynamic configuration of the vehicle continuously and dynamically. Several solutions, including the use of advanced sensors or automatic controls [12, 13], have been proposed, but shape memory alloys emerge as one of the most suitable technologies to address this evolving need [14, 15]. An example is the model developed in [16], which optimises the lifetime of the TWASE (Two-Way Assisted through SuperElasticity) actuator by limiting the maximum transformation strain based on geometric parameters. This innovative self-reversible actuator is applicable to numerous automotive systems activated by heat transfer.

These materials can undergo a definite change in shape, size, form, or properties in response to environmental stimuli such as temperature, stress, light, or magnetic fields [17]. Due to their potential for use in sensors, actuators, and adaptive systems [18], these materials are gaining increasing attention. Indeed, the paper proposes to analyse an innovative solution that significantly improves the car's aerodynamic efficiency compared to the work reported in [18], by implementing a system that is compact and lightweight, highly efficient and particularly feasible since it can be completely inserted into the car's front grill.

The SMA phenomenology, completely suitable to this engineering requirement, results from a reversible phase transformation between the two crystalline phases of shape memory alloys, namely austenite and martensite. During the reversible phase transformation between austenite and martensite, a significant change in shape and material properties of the SMA is observed due to changes in its crystal structure. Pseudo-elasticity and the shape memory effect constitute the two main characteristic phenomena of shape memory alloys (SMA). These two characteristics give SMAs qualities that make them particularly suitable for solving engineering challenges. Pseudo-elasticity manifests itself in the ability of SMAs to undergo significant deformation and return to their original shape after stress removal. The shape memory effect, on the other hand, emphasises the ability of SMAs to 'remember' and recover their original configuration after being subjected to deformation. In response to a specific stimulus, often a change in temperature, the material returns to its initial shape, exhibiting memory-like behaviour. Moreover, the shape memory effect of SMAs has been extensively studied and applied in various fields, including aerospace [19, 20], robotics [21, 22], and biomedical engineering [23, 24]. The unique properties of SMAs, such as high strength, fatigue resistance, and biocompatibility [25], have made them attractive for the development of new materials and devices.

Several studies have been conducted to examine the behaviour of these alloys under the influence of different thermal conditions. It has been observed that the temperature range for thermoelastic martensitic transformation in metals and alloys occurs at both cryogenic and environmental temperatures around 100 °C. However, sectors such as robotics, aerospace, and the oil industry require alloys capable of operating at temperatures above 120 °C. This requirement presents several challenges, including diffusion control, decomposition, recrystallisation, and recovery that cannot be neglected. Research carried out by Firstov et al. [26] indicated that it is necessary to apply precipitation processes to the austenitic state of HTSMAs (High-Temperature Shape Memory Alloys) to avoid stabilisation of martensite, thus preventing both decomposition and plastic deformation during shape recovery. In another study by Humbeeck [27], examples of the use of HTSMAs and their disadvantages, including a significant reduction in performance at temperatures of 380 °C, are illustrated, as well as patents that open up new opportunities for the use of these alloys.

In this work, the structural and the aerodynamic behaviour of an Active Grille Shutter (AGS) system has been evaluated. Indeed, active grille shutters are a promising technology for improving the aerodynamic efficiency of vehicles. These systems use movable flaps to adjust the airflow through the front grille of a car, reducing drag and improving fuel efficiency. The AGS is in the grille of the vehicle and can be opened or closed to regulate the airflow into the engine compartment. When closed, the amount of air entering the engine compartment is reduced, thus reducing the drag and improve the fuel efficiency. This effect is particularly important at higher speeds, where air resistance can have a significant impact on a vehicle's efficiency. Additionally, AGS can help to reduce the carbon footprint of a vehicle by improving its overall efficiency. Furthermore, it can help to improve the engine's performance by regulating the temperature in the engine compartment, thus ensuring a consistent temperature, and reducing wear and tear on its components. The integration of shape memory alloy (SMA) materials into active grille systems (AGS) represents a significant engineering milestone for the automotive industry. The unique characteristics of SMAs give AGSs the ability to precisely adjust their geometry, adapting to different operating conditions and effectively optimising airflow management. Integrating SMAs into AGS systems, however, is a complex engineering challenge that requires a deep understanding of material behaviour, system dynamics, and control strategies. Despite the immense potential, up to the authors knowledge, the existing literature lacks in providing a comprehensive design process, including the critical development of a SMA material user subroutine capable of accurately modelling the effects of pseudo-elasticity and shape memory. In response to these research gaps, this scientific paper aims to highlight the fundamental importance of documenting the entire workflow involved in AGS design, with a specific focus on materials.

The paper introduces an innovative solution characterized by high efficiency, compactness, and safety, enabling the Active Grille Shutter (AGS) to maintain two specific equilibrium positions under different load conditions using a bistable SMA actuator, without compromising effectiveness. Compared to existing literature, this study aims to enhance the aerodynamic drag coefficient and provide an actuation solution with low weight, small footprint, and high efficiency. The analysed component, the AGS, has been initially studied from an aerodynamic point of view to evaluate significant improvements in vehicle aerodynamics. Subsequently, the integration of the SMA actuator, supported by an in-depth phenomenological and numerical study, facilitated the development of a complete system. The research details the entire process, from the design to the analysis of the AGS handling system, with a particular focus on the materials used. Then, the numerical model employed results suitable for this solution, accurately describing the material behaviour in line with the engineering requirements. This purpose-designed system analysed in the research has the potential to improve vehicle efficiency by approximately 4% at a speed of 140 km/h.

In "Theoretical Foundation and Numerical Modelling of SMA Constitutive Law" section, a theoretical background on shape memory alloys is presented. In "Numerical Application: Active Grille Shutter Modelling" section, the application to the design of the bistable actuator for the AGS system and an in-depth discussion of the thermomechanical behaviour of SMA springs is introduced and commented. Conclusions are reported in "Conclusions" section.

Theoretical Foundation and Numerical Modelling of SMA Constitutive Law

The chapter is dedicated to an in-depth study of the theoretical background and numerical modelling of the constitutive law of shape memory alloys. Its objective is to provide a comprehensive overview of the principles governing the behaviour of SMAs, focussing on the formulation of a constitutive law that can accurately describe their distinctive mechanical and thermal responses for engineering contexts.

Theoretical Background

The main characteristics of the shape memory alloys are related to the variation of the internal crystalline structure depending on the mechanical or thermal load. The two phases, present in these alloys, are the austenitic phase and the martensitic phase. Austenite is stable at high temperatures and has a central body cubic symmetry lattice (BCC) where Titanium atoms occupy the vertices of the two cubic lattices. Martensite is the stable phase at low temperatures. It has a disordered structure; this phase exhibits greater flexibility compared to the austenitic phase, enabling it to endure substantial deformations without chemical bond breakage. The transformation between the two phases gives rise to two primary effects in shape memory alloys, namely, the pseudoelastic effect (PE) and the shape memory effect (SME).

The model used for the numerical implementation of the thermomechanical behaviour of shape memory alloys is the Brinson model. This model provides a robust theoretical framework for the analysis and simulation of the unique responses of SMAs, contributing to the detailed understanding of their constitutive properties [28].

The phase diagram (Fig. 1) is a central tool for understanding and predicting the thermomechanical behaviour under varying temperature and stress conditions. This diagram illustrates the different stages in which SMA can exist at different levels of temperature and stress. Four different areas corresponding to different states of the material can be identified. In region 1, the combination of high stress and low temperature results in detwinned Martensite phase. The twinned Martensite which forms while cooling below Ms under stress-free conditions is present in region 2. In the mid- region 3, the alloy can be found both in the Austenite or Martensite phases, while in region 4, characterized by high temperature and low stress, the alloy is in Austenite phase.

According to the phase diagram, C^*_{AM} and C^*_{MA} are the band slope for forward and reverse phase transformations in the (σ, T) diagram, while σ_{scr} and σ_{fcr} are the austenite to martensite critical stress value for start and end of the phase transformation. The thermomechanical properties of alloys are examined based on the previously described diagram. The alloy's response varies depending on its initial temperature state before undergoing mechanical or thermal deformation.

In a condition of high temperature ($T \geq A_f$), a stress addition leads to the phase transition from the Austenite to the Martensite phase. However, the stress removal leads to the reverse transition from the Martensite to the Austenite phase, resulting in no residual strain, according to the stress–strain diagram in Fig. 2.

Instead, during the loading and unloading phase in a condition of low temperature ($T \leq A_f$), a residual deformation can be appreciated in the shape material alloy and can be recovered by a thermal load.

FEM Implementation: User Material Subroutine

To introduce the thermomechanical behaviour of shape memory alloys in commercial finite element environment, a user material has been implemented. Both properties of shape memory alloys are required for the application

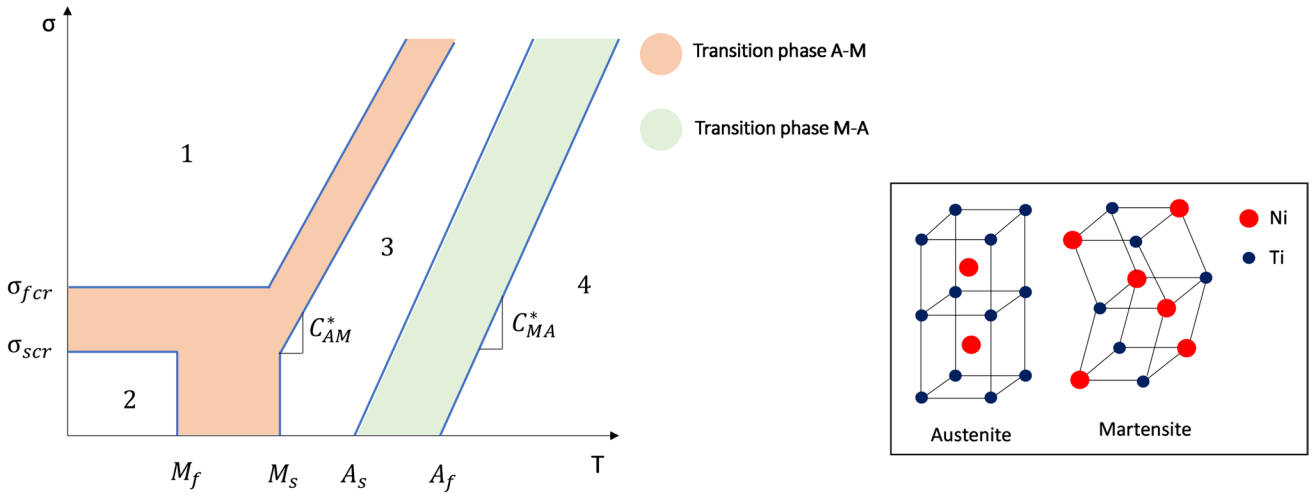

Fig. 1 Phase diagram of a shape memory alloy (σ-T diagram phase)

analysed in this research, so a numerical model replicating the analytical thermomechanical model becomes mandatory. The UMAT subroutine has been implemented in the Abaqus standard finite element code environment to include both effects and evaluate the crystallographic phase, stress, and strain conditions related to a thermomechanical load. The routine consists of three sequential macro blocks (see Fig. 3).

Material Properties and Stiffness Matrix Calculation

First of all, the material properties are calculated: Young's modulus and Poisson's modulus. These moduli are given by Eqs. (1) and (2):

$$E = \xi E_M + (1-\xi)E_A \tag{1}$$

$$\nu = \xi \nu_M + (1-\xi)\nu_A, \tag{2}$$

where E_M is the martensite Young's modulus, E_A is the austenite Young's modulus, ν_M is the martensite Poisson's modulus, ν_A is the austenite Poisson's modulus, and ξ is the martensite volume fraction.

After, elastic stiffness tensor is calculated. The assembly of the stiffness matrix of the whole model is a match between the Austenite stiffness matrix and Martensite stiffness matrix, weighted average with the total volume fraction of martensite ξ. The compliance matrix of the whole model is an average of $[S_M]$ and $[S_A]$:

$$[S] = \xi[S_M] + (1-\xi)[S_A], \tag{3}$$

where $[S_M]$ and $[S_A]$ are Martensite compliance matrix and Austenite compliance matrix, respectively, given by following equations:

$$[S_M] = \begin{bmatrix} \frac{1}{E_M} & -\frac{\nu_M}{E_M} & -\frac{\nu_M}{E_M} & 0 & 0 & 0 \\ -\frac{\nu_M}{E_M} & \frac{1}{E_M} & -\frac{\nu_M}{E_M} & 0 & 0 & 0 \\ -\frac{\nu_M}{E_M} & -\frac{\nu_M}{E_M} & \frac{1}{E_M} & 0 & 0 & 0 \\ 0 & 0 & 0 & \frac{1}{G_M} & 0 & 0 \\ 0 & 0 & 0 & 0 & \frac{1}{G_M} & 0 \\ 0 & 0 & 0 & 0 & 0 & \frac{1}{G_M} \end{bmatrix} \tag{4}$$

$$[S_A] = \begin{bmatrix} \frac{1}{E_A} & -\frac{\nu_A}{E_A} & -\frac{\nu_A}{E_A} & 0 & 0 & 0 \\ -\frac{\nu_A}{E_A} & \frac{1}{E_A} & -\frac{\nu_A}{E_A} & 0 & 0 & 0 \\ -\frac{\nu_A}{E_A} & -\frac{\nu_A}{E_A} & \frac{1}{E_A} & 0 & 0 & 0 \\ 0 & 0 & 0 & \frac{1}{G_A} & 0 & 0 \\ 0 & 0 & 0 & 0 & \frac{1}{G_A} & 0 \\ 0 & 0 & 0 & 0 & 0 & \frac{1}{G_A} \end{bmatrix}, \tag{5}$$

where G_A and G_M are Austenite shear modulus and Martensite shear modulus, respectively. Finally, the stiffness matrix $[R]$ is calculated as inverse matrix of $[S]$:

$$[R] = [S]^{-1} \tag{6}$$

Phase Diagram and Stress–Strain Relationship

The second step provides the stress–strain relationship formulation starting from phase diagram of shape memory alloys. There are two cases, addicted to value of T^*.

The first case is when the shape memory alloys temperature T^* is less than Austenite finish temperature A_f as

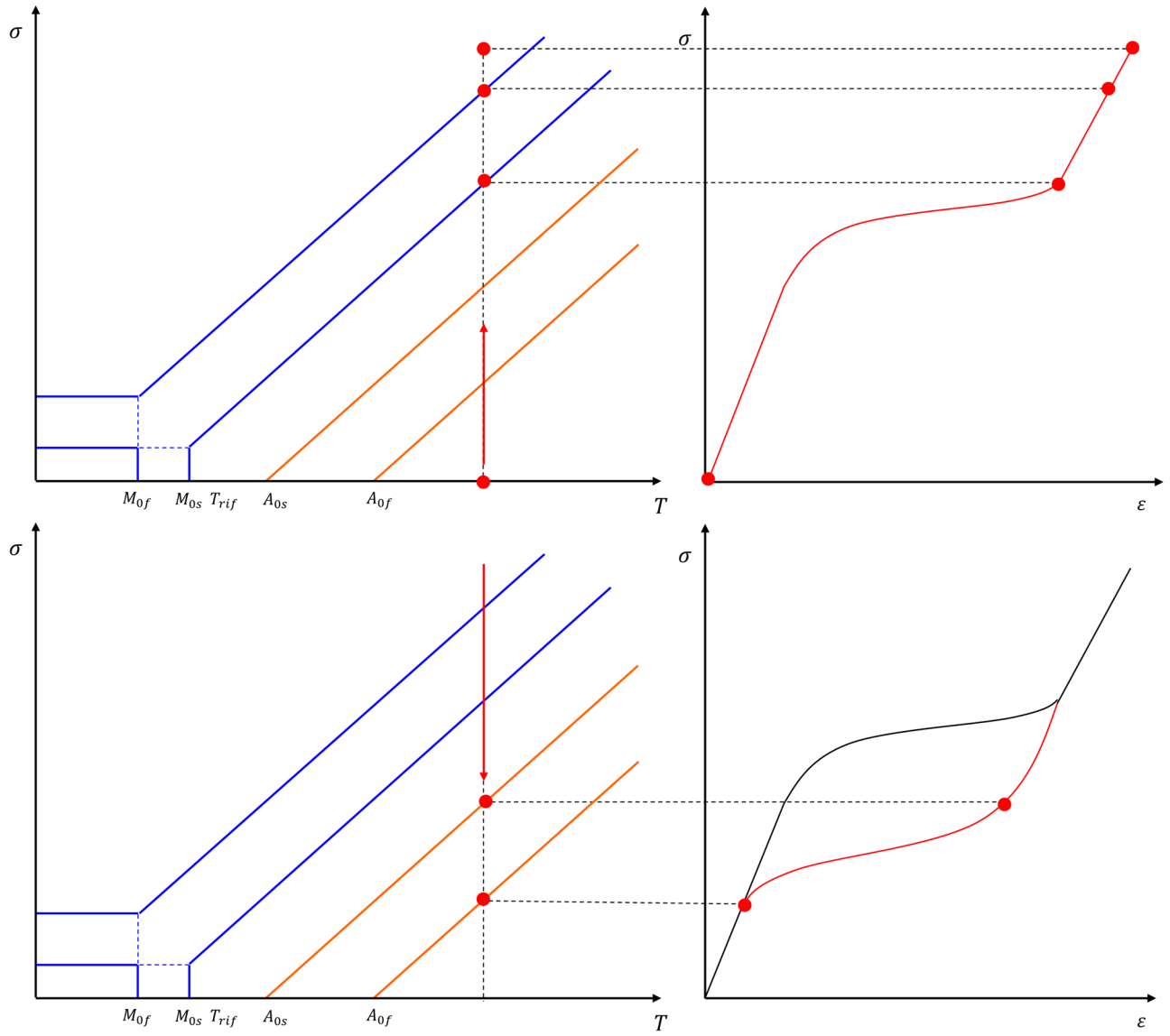

Fig. 2 Pseudoelastic behaviour

represent in Fig. 4. The values of σ_M^s and σ_M^f are given by following equations:

$$\begin{cases} \sigma_M^s = \sigma_{scr} \\ \sigma_M^f = \sigma_{fcr} \end{cases} T^* \leq M_s \tag{7}$$

$$\begin{cases} \sigma_M^s = \sigma_{scr} + C_M\left(T^* - M_s\right) \\ \sigma_M^f = \sigma_{fcr} + C_A\left(T^* - M_s\right) \end{cases} M_s < T^* \leq A_s \tag{8}$$

where σ_{scr},σ_{fcr},C_M, C_A,and M_s are features of material and they are input for user subroutine. As a result, the stress–strain relationship is obtained as showed as shown in Fig. 5. The values of ε_A and ε_B are given by:

$$\varepsilon_A = \frac{\sigma_M^s}{E_A} \tag{9}$$

$$\varepsilon_B = \frac{\sigma_M^f}{E_M} + \varepsilon_l \tag{10}$$

where E_A, E_M, and ε_l are features of material and they are input for user subroutine.

The second case is when the shape memory alloys temperature T^* is greater than Austenite finish temperature A_f as represented in Fig. 6. The values of σ_M^s a σ_M^f are given by Eqs. (7) and (8), while the values of σ_A^s and σ_A^f are given by following equations:

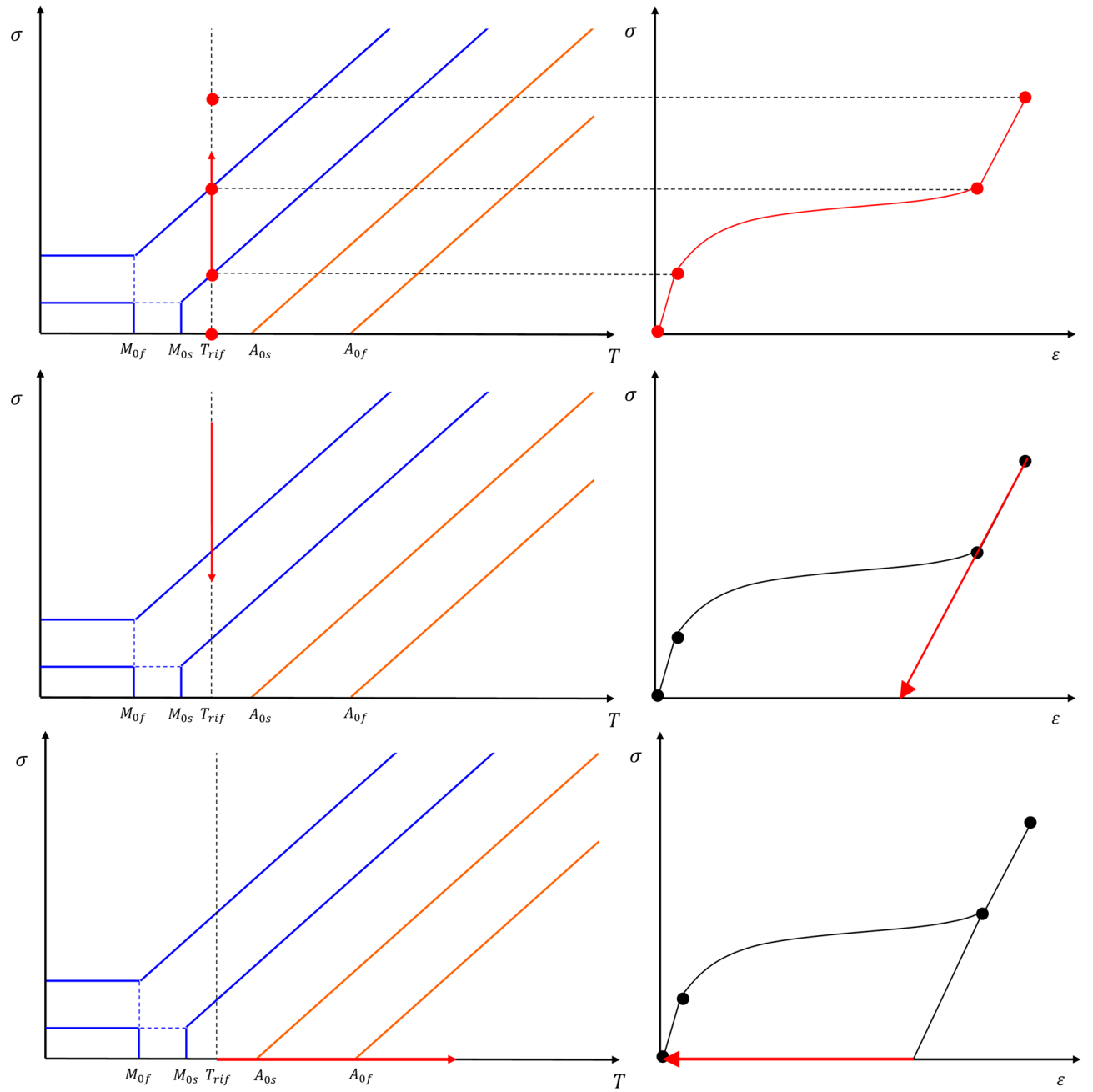

Fig. 3 Shape memory effect

$$\begin{cases} \sigma_A^s = C_A\left(T^* - A_s\right) \\ \sigma_A^f = C_A\left(T^* - A_f\right) \end{cases} \tag{11}$$

where A_s and A_f are features of material and they are input for user subroutine. As a result, the stress–strain relationship is obtained as showed in Fig. 7.

The values of ε_A and ε_B are given by Eqs. (9) and (10), while ε_D and ε_E are given by following equations:

$$\varepsilon_D = \frac{\sigma_A^s}{E_M} + \varepsilon_l \tag{12}$$

$$\varepsilon_E = \frac{\sigma_A^f}{E_A} \tag{13}$$

In this case, it is not necessary the thermic return, because the hysteresis loop is closed. This situation means that the material, after the application of a load, returns

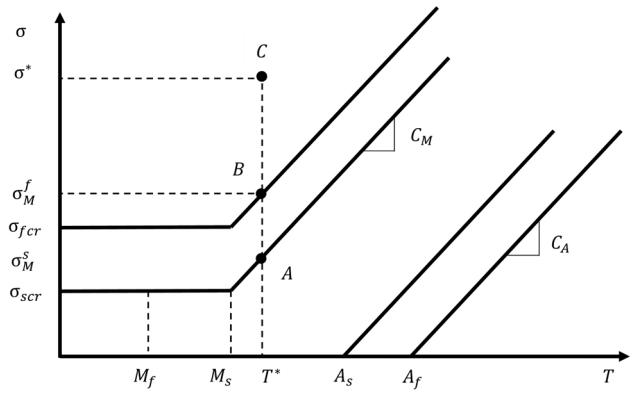

Fig. 4 Individuation of key point on SMA phase diagram (Case 1)

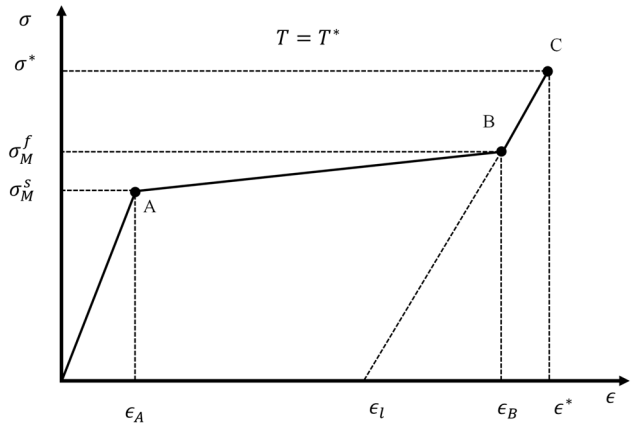

Fig. 5 Stress–strain relationship (shape memory effect)

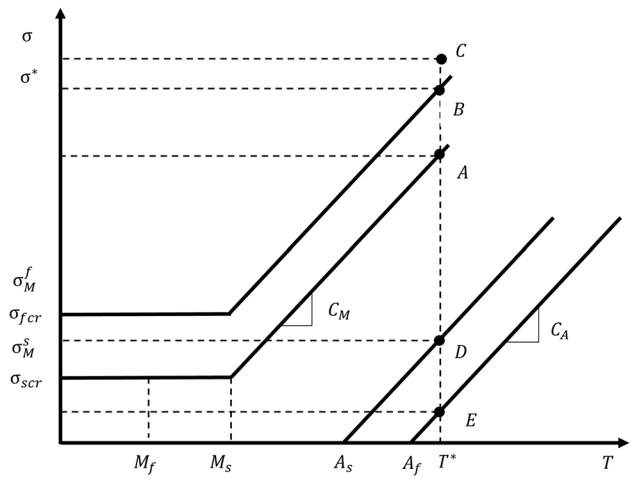

Fig. 6 Individuation of key point on SMA phase diagram (Case 2)

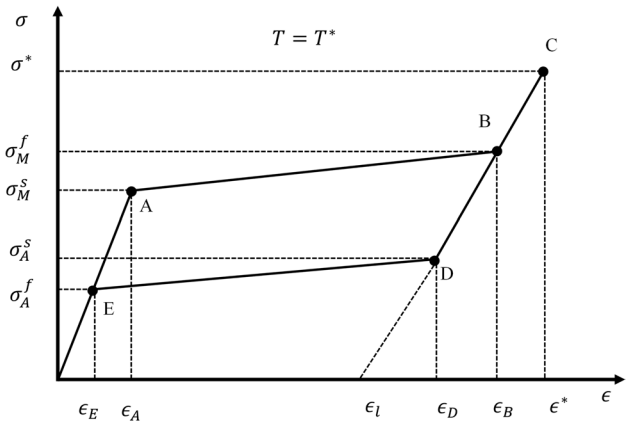

Fig. 7 Stress–strain relationship (pseudoelastic behaviour)

automatically to its start configuration as soon as the load is removed.

Thermal Matrix and Refresh of Strain and Stress

Every step, the UMAT refreshes the strain and the stress of the whole model also considering the temperature variation. The thermal matrix $[K_T]$ is given by following equation:

$$[K_T] = \xi[K_M] + (1-\xi)[K_A], \tag{14}$$

where

$$[K_M] = \begin{bmatrix} \frac{\alpha_M E_M}{1-2\upsilon_M} & 0 & 0 & 0\ 0\ 0 \\ 0 & \frac{\alpha_M E_M}{1-2\upsilon_M} & 0 & 0\ 0\ 0 \\ 0 & 0 & \frac{\alpha_M E_M}{1-2\upsilon_M} & 0\ 0\ 0 \\ 0 & 0 & 0 & 0\ 0\ 0 \\ 0 & 0 & 0 & 0\ 0\ 0 \\ 0 & 0 & 0 & 0\ 0\ 0 \end{bmatrix} \tag{15}$$

$$[K_A] = \begin{bmatrix} \frac{\alpha_A E_A}{1-2\upsilon_A} & 0 & 0 & 0\ 0\ 0 \\ 0 & \frac{\alpha_A E_A}{1-2\upsilon_A} & 0 & 0\ 0\ 0 \\ 0 & 0 & \frac{\alpha_A E_A}{1-2\upsilon_A} & 0\ 0\ 0 \\ 0 & 0 & 0 & 0\ 0\ 0 \\ 0 & 0 & 0 & 0\ 0\ 0 \\ 0 & 0 & 0 & 0\ 0\ 0 \end{bmatrix}$$

where α_M and α_A are Martensite expansion coefficient and Austenite expansion coefficient, respectively.

The current compliance matrix with all the updating strain and stress (thermal and mechanical) $[S_1]$ is refreshed as follow:

$$[S_1] = [S_1] + [dS], \tag{16}$$

where $[dS]$ is the increment of the compliance matrix.

The increment of the compliance matrix in given by following equation:

$$[dS] = \left[dS_M\right] + \left[K_T\right]\left(T_1 - T^*\right) + \left[dK_T\right](T_1 - T_0), \quad (17)$$

where $\left[dS_M\right]$ is the increment of compliance matrix referred only to a mechanical behaviour, T_1 is the current temperature, T_0 is the temperature of previous step, and $\left[dK_T\right]$ is the increment of thermal matrix given by following equation:

$$\left[dK_T\right] = d\xi\left(\left[K_M\right] - \left[K_A\right]\right) \quad (18)$$

Numerical Application: Active Grille Shutter Modelling

AGS Aerodynamic Requirements

As previously mentioned, AGS technology is widely studied in the automotive aerodynamic optimization field, as it offers promising advantages, especially in terms of drag coefficient reduction.

The chosen case study is a segment-B vehicle that does not feature AGS technology, but only a front grill.

The objective of the work is to replace the front grill with an aesthetic AGS, whose blades can rotate allowing the vehicle to work in two stable conditions:

- *AGS open*: a configuration that allows the flow to enter in the front underhood guaranteeing the correct engine cooling in the vehicle.
- *AGS closed*: a configuration that does not allow the flow to enter in the front underhood, significantly reducing the amount of air in the engine compartment. This configuration can be used at high speeds to reduce the drag force, without efficiency losses in the engine cooling function.

CFD simulations have been thus carried out to define the drag reduction that can be obtained with the introduction of the AGS on the vehicle. The numerical method consists of steady RANS, using *k-ε* for turbulence modelling,

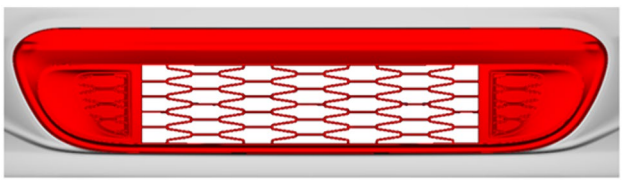

Fig. 8 Case study front grill

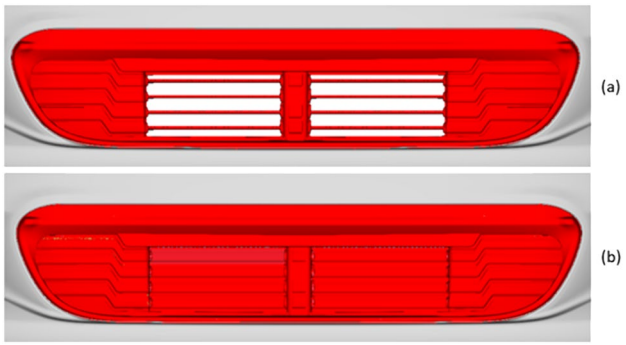

Fig. 9 AGS introduced. **a** Open configuration; **b** closed configuration

considering an inlet velocity of 140 kph to simulate the behaviour of the vehicle at high speeds (see Figs. 8, 9).

The three configurations have been then analysed to verify the aerodynamic performances:

From Table 1 and Fig. 10, it is possible to observe that the replacement of the front grill with the AGS geometry has an effect on the vehicle aerodynamics, with a reduction of C_x of about 0.9% due to the new geometry.

The real contribution, however, is given by the third configuration: the blades close the lower frontal intake, reducing the amount of air entering the engine compartment, resulting in a lower contribution of the engine components on drag and yielding an overall C_x reduction of 4.1%. The impact of the blades closure on vehicle aerodynamics can be observed also from the accumulated C_x plot in the open and closed configuration (Fig. 11).

Figure 12 (area A) illustrates that the closed configuration exhibits a notably higher initial peak. This is because the flow impacts the vehicle without the opportunity for redirection into the engine compartment, leading to a consequent enlargement of the stagnation area. The situation is reversed inside the engine compartment: the reduction of the amount of air in the front underhood leads to a strong C_x reduction on both the front vehicle components (Fig. 12, area B) and the firewall (Fig. 12, area *C*). There are no appreciable differences in the curve behaviour for the middle and rear part of the vehicle. Thus, the gain achieved in the front part is also visible in the total vehicle drag coefficient, which is approximately 4.1% lower than the base model and about 3.3% lower than the open configuration, proving that the

Table 1 Drag coefficient C_x results on the analysed configurations

	C_x	Delta C_x (%)
Base model—front grill	0.324	–
AGS—open configuration	0.321	− 0.9
AGS—closed configuration	0.310	− 4.1

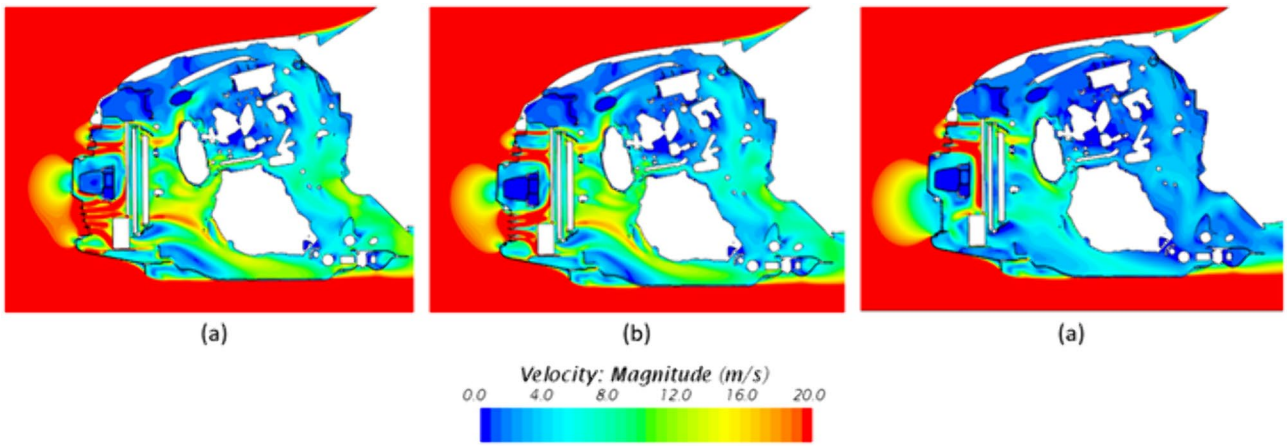

Fig. 10 Velocity magnitude contour on section plane $y = -0.1$ m for the three configurations: base model (**a**)—open configuration (**b**)—closed configuration (**c**)

Fig. 11 Accumulated C_x on the vehicle for open configuration (blue) and closed configuration (orange) (Color figure online)

AGS introduction is a very useful solution for aerodynamic performances.

Geometrical Description

Once it has been confirmed through aerodynamic analysis that the drag coefficient was an improvement, the focus moved to the design and FEM analysis of a mechanism capable of satisfying this requirement. In this context, the decision to integrate SMA's bistable actuator technology has been made to develop a system that could respond effectively and efficiently.

Bistable actuators represent a category of actuators capable of maintaining a position without continuous power consumption. These actuators employ magnetic or mechanical latching mechanisms to sustain their position, meaning power is only needed for transitioning between their two stable states. This feature renders them exceptionally energy-efficient when contrasted with other actuator types that demand a continuous power supply to uphold their position. For SMAs, which undergo continuous loading cycles, fatigue considerations are crucial for optimizing related applications. A SMA actuator's lifespan involves evaluating two types of fatigue: structural fatigue, leading to catastrophic failure, and functional fatigue, causing permanent changes in geometry and performance [29]. Chemisky et al.'s phenomenological model [30] accurately simulates both functional and structural fatigue, integrating damage accumulation and transformation-induced plasticity. This research does not incorporate the effects of fatigue, concentrating on proposing a space-saving and highly efficient solution to reduce drag.

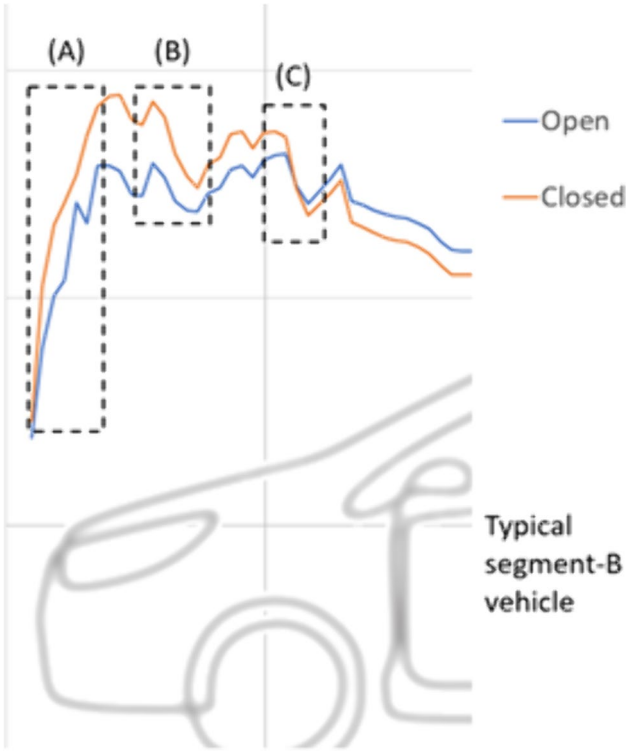

Fig. 12 Zoom on front accumulated C_x for open configuration (blue) and closed configuration (orange) (Color figure online)

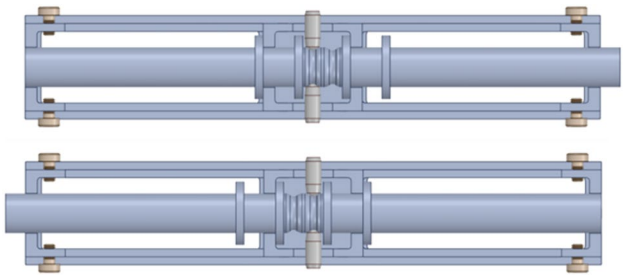

Fig. 13 Bistable SMA actuator

As a useful mechanism for moving the AGS, the bistable actuator designed and patented described in [31] is studied and evaluated in the entire context of this adaptive system. Specifically, the SMA springs operate in opposing phases, ensuring the necessary actuation force for the mechanism. Upon activation of one of the two SMA springs, the system transitions to the second equilibrium position, and vice versa. The two equilibrium positions are depicted in Fig. 13.

The main components of the AGS system are depicted in Fig. 14. The two SMA springs responsible for the linear movement of the actuator are highlighted in green and red, emphasizing their significance in the overall system. The actuator is connected to the array of fins through a gear mechanism, which converts linear motion into rotational movement.

The boundary conditions of the entire system are summarized in Fig. 16a.The motion is imposed by the actuator stroke (Fig. 15a) and is transferred to the shutters through the tooth wheel system in Fig. 15-b. Subsequently, motion is transferred to the shutters through the red connection in Fig. 15c. The main function of this connection is to simultaneously rotate all six remaining shutters in red in Fig. 15d (the first two are directly connected to the motion of the actuator). The mechanism has been designed specifically for this research, with several configurations conducted previously, but the one presented in this study proved to be the most effective. This custom-designed mechanism not only reduces the stresses on the various parts of the system, but also ensures the proper functioning of the movement.

Kinematic Results

The numerical process that validated the design of the system just described underwent a series of preliminary steps. Before proceeding to the complete analysis, all individual effects have been carefully examined and evaluated in detail. In particular, the simulations of the thermomechanical behaviour of the SMA actuated AGS can be divided into three stages. In the first stage, the force needed to move the mechanism is computed. A finite element analysis (FEM) has been carried out, with an imposed displacement of 5mm on the central body of the actuator. At this stage, the SMA springs have not been included in the analysis.

The aerodynamic moments are derived directly from the aerodynamic analyses illustrated above. Figure 16 clearly shows the application positions and the labels corresponding to each moment applied. On the right of the figure, the associated values are shown in detail, which have been incorporated into the FEM analyses.

Figure 17 provides a force-displacement graph, illustrating the maximum force required for the mechanism to move. The graph highlights several peaks, related to the movements of the mechanism of the gear wheel, which is responsible for the movement. The maximum force peak, of approximately 53N, occurs just before half of the displacement (2mm). This phenomenon is related to the need to overcome the resistance of the locking mechanism, both during overcoming the geometric curve and during the release of the lateral springs.

The purpose of this analysis is to evaluate the load transmitted by the tooth wheel system on a model without the SMA spring. Figure 18 shows the contour plot of stress distribution on the deformed shapes of actuator. The maximum stress value is located on the actuator axis at the lateral spring transition.

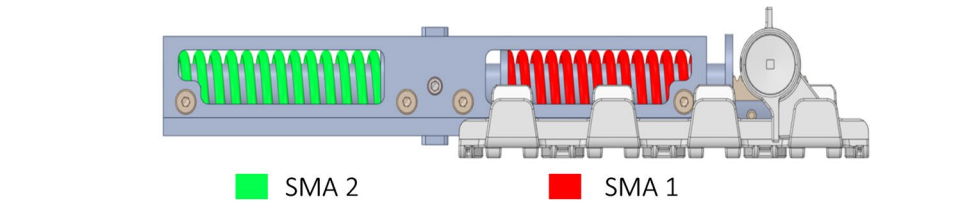

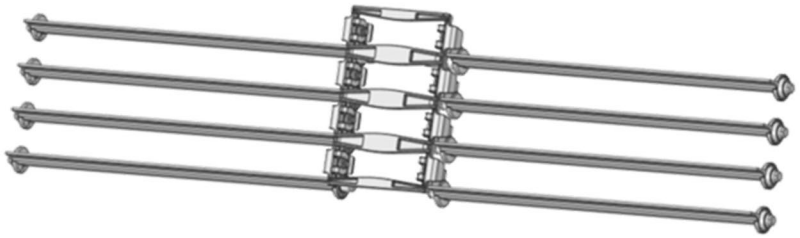

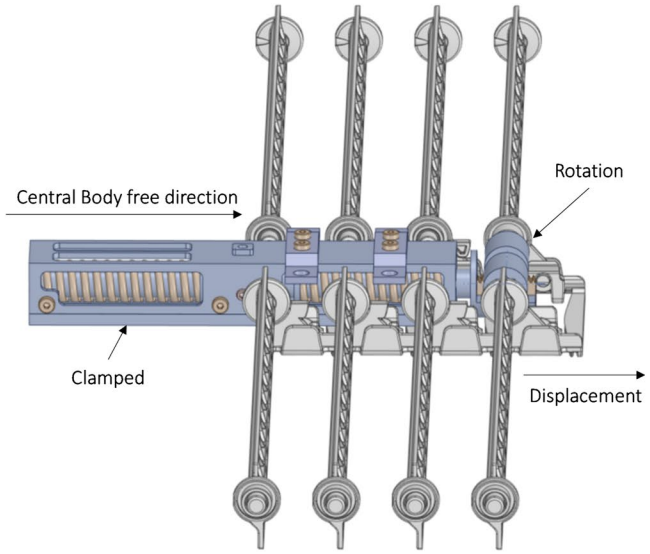

(a)

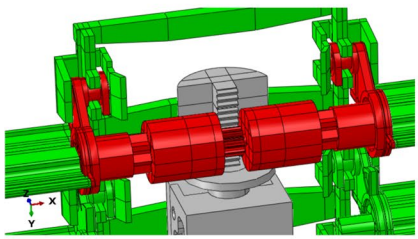

(b)

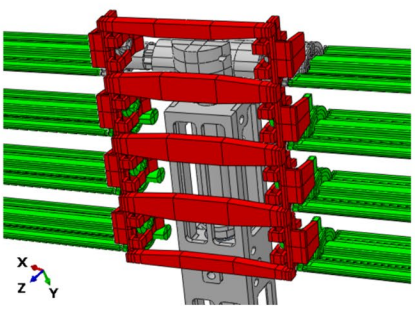

(c)

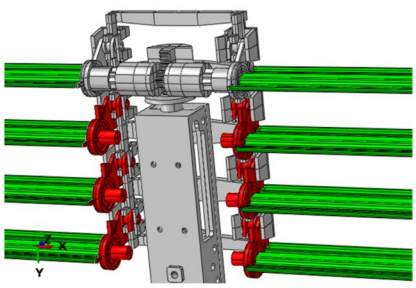

(d)

Fig. 14 Main component of the AGS system

Fig. 15 Cinematics—(**a**) tooth wheel system; (**b**) rigid movement of all shutters; (**c**) rotation of the shutters

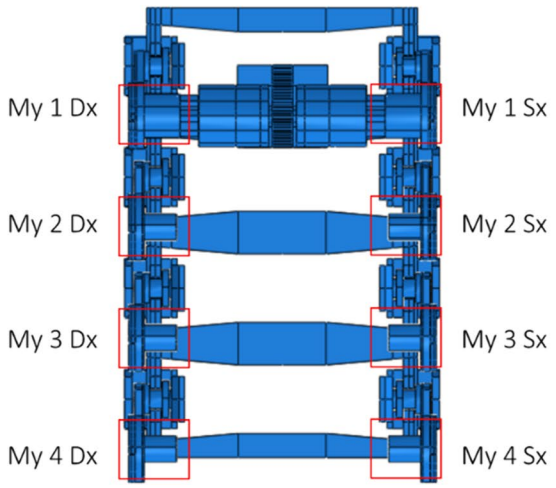

Aerodynamic Moments	
$M_y1\ Dx\ [N\ mm]$	7.66
$M_y2\ Dx\ [N\ mm]$	11.8
$M_y3\ Dx\ [N\ mm]$	8.53
$M_y4\ Dx\ [N\ mm]$	−0.74
$M_y1\ Sx\ [N\ mm]$	7.18
$M_y2\ Sx\ [N\ mm]$	12
$M_y3\ Sx\ [N\ mm]$	8.66
$M_y4\ Sx\ [N\ mm]$	−0.705

Fig. 16 Aerodynamic moments on blades

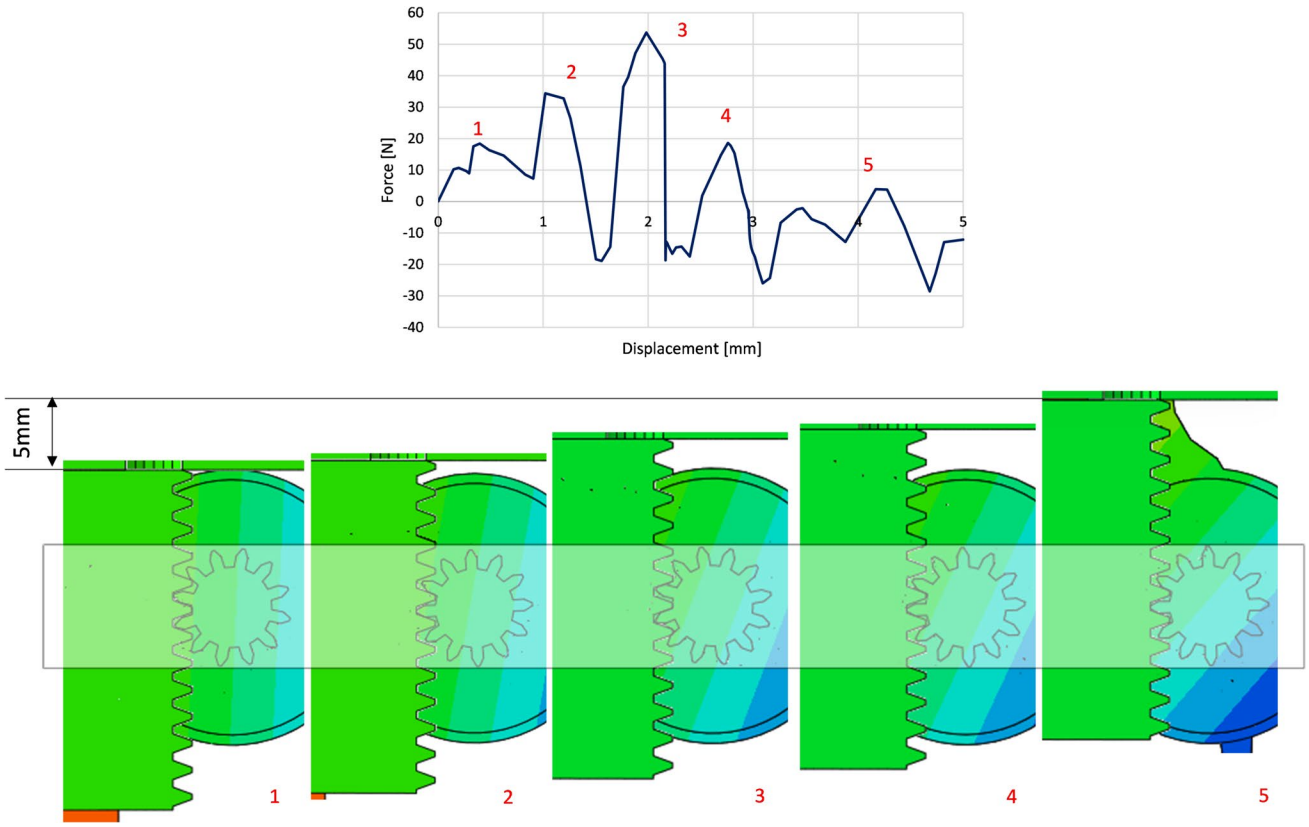

Fig. 17 Force—displacement

Thermomechanical Analysis on a SMA Spring

The second stage of the analysis focuses on evaluating the maximum force exerted by the SMA springs during a full Martensite-Austenite phase transition. The analysis has been carried out on a SMA spring (length of 105mm, 15 coils and diameter of 2.7mm) fully constrained at one edge. Initially, a mechanical load has been applied to the spring in the form of a displacement of 55 mm. This brought the spring to the stress value of σ_f^M, enabling a transformation into Martensite phase. The

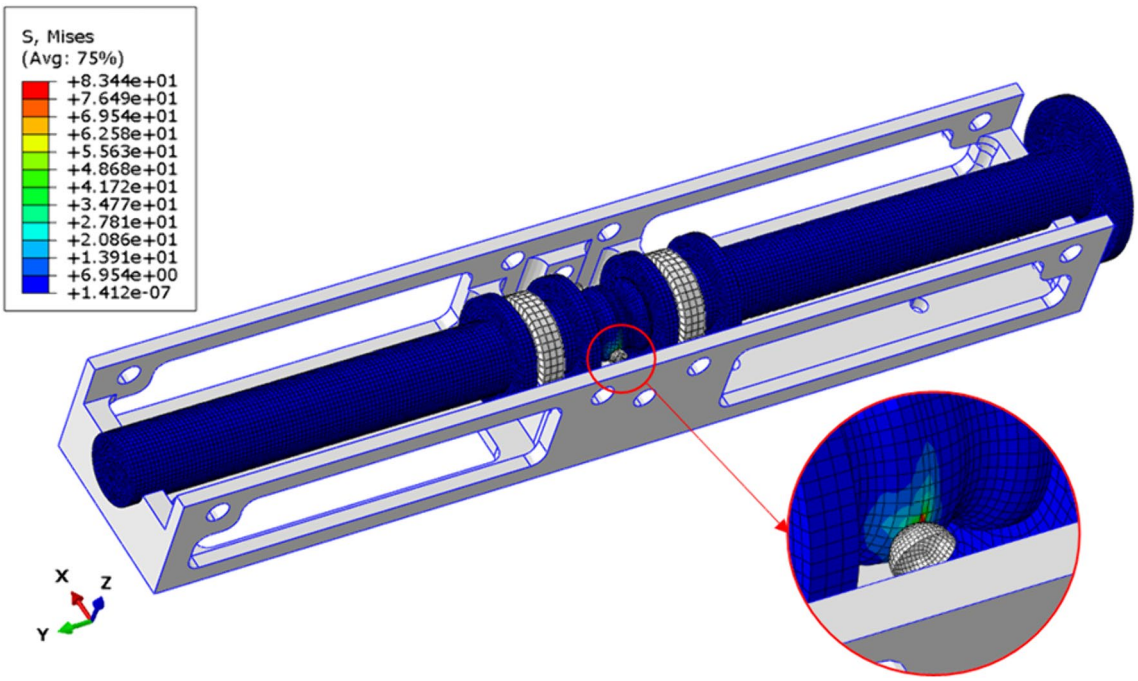

Fig. 18 Von Mises distribution

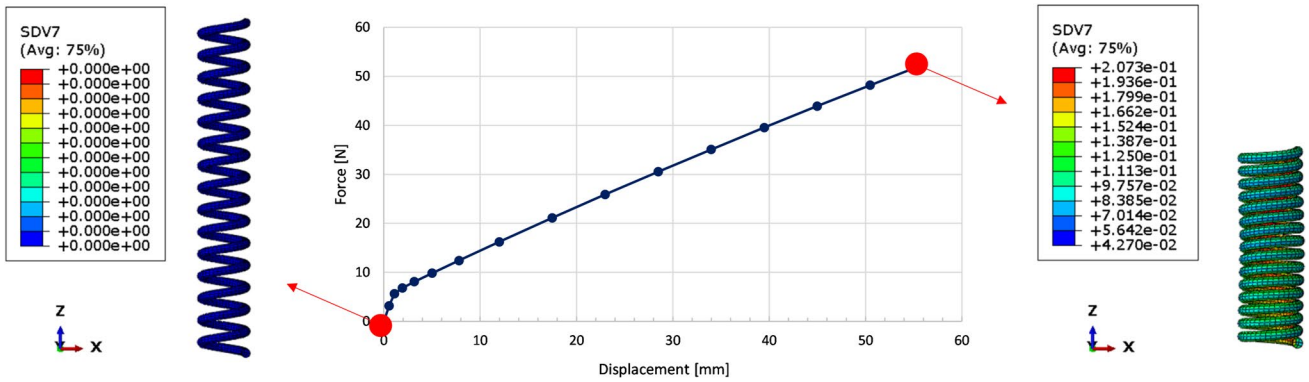

Fig. 19 SMA spring. Force—displacement during compression load

thermomechanical properties of the adopted materials are NiTiNOL for SMA springs which are reported in [18, 32, 33], aluminium for central body, hemispheres, and hinges, and ABS for AGS.

According to Fig. 19, the material in the spring is not completely converted into martensite, meaning that it is possible to optimise the geometric characteristics of the spring to maximize its efficiency in relation to the load. The force exerted by the spring during the mechanical loading phase remains in the transformation plateau and does not reach the martensite transformation (Fig. 19). In addition, the value of the volume fraction of martensite (SDV7) on the SMA spring during the loading phase is presented. Through these visual representations, it is evident how the SMA spring manifests a progressive increase in the volume fraction along its structure during the loading process.

During the heating phase, a partial recovery of deformation takes place. In Fig. 20, the time history of the spring during the three phases (loading, unloading, and heating) is shown. During the unloading phase, when the spring stabilises, it recovers approximately 20% of the applied load, while during the heating phase, the spring recovers 90% of the initial deformation. A higher heating temperature would have resulted in full recovery of the deformations. From the analysis of the figure, it is also evident that the volumetric fraction of martensite does not reduce to zero during the heating phase, although it shows a significant decrease compared to the condition when the spring is unloaded.

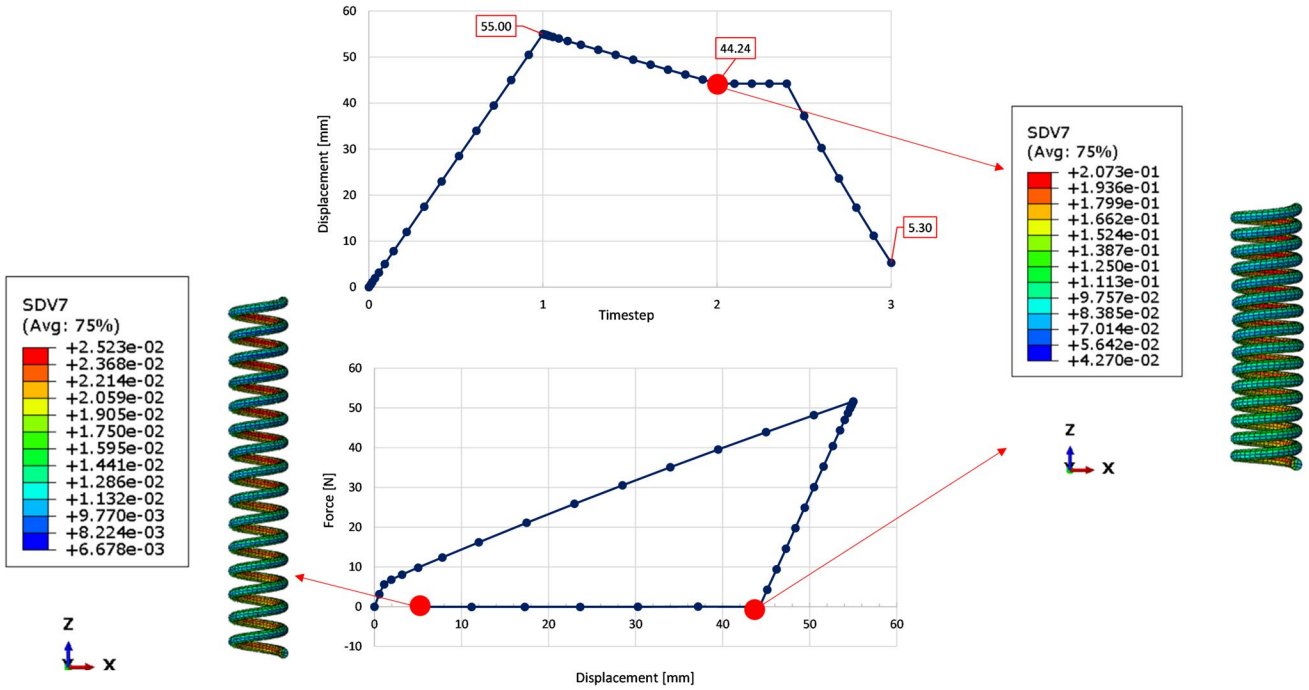

Fig. 20 SMA spring. Partial recovery of deformation

Moreover, during the heating phase, as the spring goes from a temperature of 25 °C to a temperature of 100 °C, the spring can exert a force of 112N. The two springs, in phase opposition, exert an equilibrium force of approximately 51N each. Therefore, the extra force of the SMA springs during the heating phase is approximately 61N, which is higher than the value required to move the mechanism.

AGS Results

In the third stage, a complete verification of the SMA actuated AGS has been performed through a simulation involving all components, boundary conditions, and loading conditions. The simulation has been carried out in eight steps. First, a preload has been applied to the SMA spring until full transition to the Martensite phase is achieved. During this stage, the AGS system has been kept blocked by the locking mechanisms. Next, the two side springs arranged radially to the actuator axis by 180° have been pre-compressed by a displacement of 0.529mm. After this, the release of the lateral springs took place in a separate step. In the subsequent step, aerodynamic moments are exerted on each shutter of the AGS. The fifth step involves the heating phase, where a temperature of 100 °C has been considered. To evaluate the entire mechanism, the functioning of both springs has been validated. Hence, after the first spring is heated and activated, it is cooled down, allowing the second spring to be activated. The entire workflow is reported in Fig. 21.

In Fig. 22, the main four configurations of the SMA actuated AGS, resulting from the eight steps, are introduced. From the figure, it emerges that there are no critical problems with the movement of the mechanism. In the detailed analysis of the AGS, two key factors have been considered: the SMA springs and the aerodynamic moments. Movement is only guaranteed by the temperature increase applied to the SMA springs. From the displacement plots, it can be seen that the springs are able to provide the force required to lock and unlock the mechanism in both positions.

Conclusions

In this study, an innovative solution has been presented to improve aerodynamic performance for an automotive application without compromising the efficiency and weight of a vehicle. The research is based on the movement of a Grille Shutter, which employs a bistable SMA actuator to modify the movable flaps into two equilibrium positions without requiring continuous power supply. The system has been subjected to extensive numerical verification to ensure that the required forces, SMA spring temperatures, and movement are optimal for the proposed solution. The adoption of shape memory alloys as the actuation mechanism has been particularly advantageous, as these smart materials are well suited to these requirements. Indeed, the constitutive model of the smart materials described allows the effects of shape memory and pseudo-elasticity to be replicated, meeting the

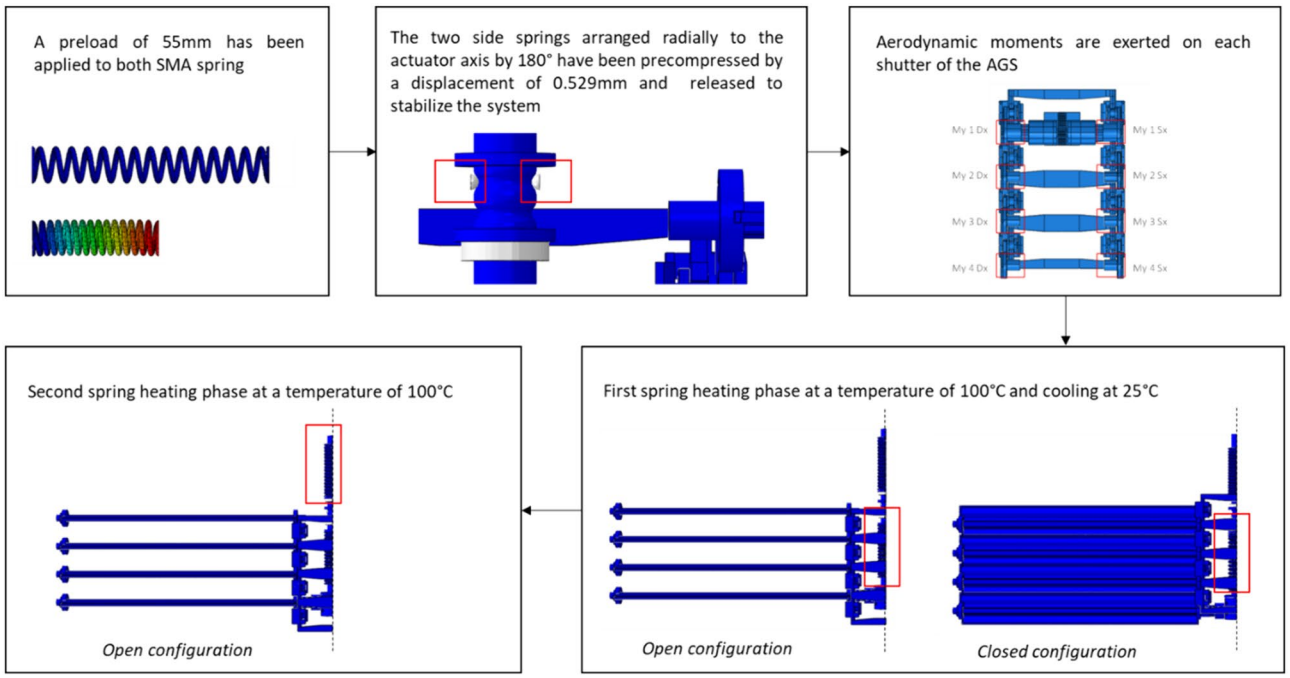

Fig. 21 Entire FEM analysis workflow

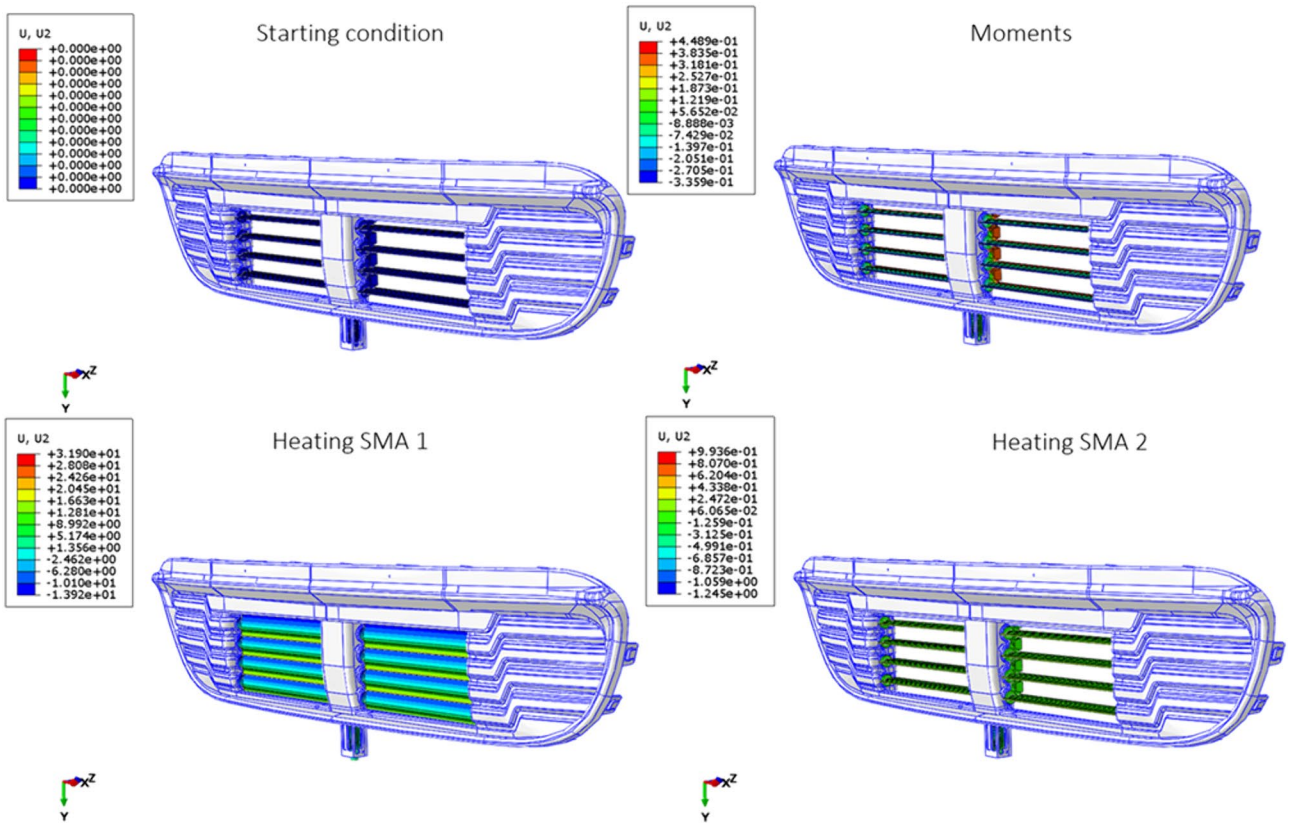

Fig. 22 SMA actuated AGS full simulation. Displacement distribution. **A**: starting condition, **B**: moments, **C**: heating—SMA 1, **D**: heating—SMA 2

specific requirements of engineering applications. Through careful numerical analysis focussing on materials, movement, and forces, the study demonstrated the effectiveness of the SMA springs in rotating the AGS fins 90°, meeting aerodynamic load requirements and achieving a significant 4% reduction in Cx compared to reference models. These results highlight the potential of this research in advancing adaptive aerodynamics, offering valuable insights into the practical applications of SMA technology within complex systems.

Data availability

The data that support the findings of this study are available from the corresponding author upon reasonable request.

References

1. Qiu J, Wang C, Huang C, Ji H, Xu Z (2014) Smart skin and actuators for morphing structures. Procedia IUTAM 10:427–441
2. Weisshaar TA, Duke DK (2006) Induced drag reduction using aeroelastic tailoring with adaptive control surfaces. J Aircr 43(1):157–164
3. Bowman J, Sanders B, Cannon B, Kudva J, Joshi S, Weisshaar T (2007) Development of next generation morphing aircraft structures. In 48th AIAA/ASME/ASCE/AHS/ASC structures, structural dynamics, and materials conference, p 1730
4. Dai P, Yan B, Huang W, Zhen Y, Wang M, Liu S (2020) Design and aerodynamic performance analysis of a variable-sweep-wing morphing waverider. Aerosp Sci Technol 98:105703
5. Parsons WP, Gasparetto VE, ElSayed MS, Saad M, Shield S, Brown GL, Hilliard LM (2022) Dynamic aeroelastic performance optimization of adaptive aerospace structures using structural geometric nonlinearities. J Aerosp Eng 35(6):04022089
6. Weisshaar TA (2006) Morphing aircraft technology-new shapes for aircraft design. Multifunctional structures/integration of sensors and antennas, O1–1
7. Ivanco T, Scott R, Love M, Zink S, Weisshaar T (2007) Validation of the Lockheed Martin morphing concept with wind tunnel testing. In 48th AIAA/ASME/ASCE/AHS/ASC structures, structural dynamics, and materials conference, p 2235
8. Huminic A, Huminic G (2012) Numerical flow simulation for a generic vehicle body on wheels with variable underbody diffuser (No. 2012-01-0172). SAE Technical Paper
9. Nath DS, Pujari PC, Jain A, Rastogi V (2021) Drag reduction by application of aerodynamic devices in a race car. Adv Aerodyn 3(1):1–20
10. Çiftçi H, Bayindirli C, İlker ÖRS (2023) Experimental investigation of spoiler application in an SUV type vehicle. Int J Energy Appl Technol 10(1):1–5
11. Palanivendhan M, Chandradass J, Saravanan C, Philip J, Sharan R (2021) Reduction in aerodynamic drag acting on a commercial vehicle by using a dimpled surface. Mater Today Proc 45:7072–7078
12. Piechna J (2021) A review of active aerodynamic systems for road vehicles. Energies 14(23):7887
13. de Carvalho Pinheiro H, Russo F, Sisca L, Messana A, De Cupis D, Ferraris A et al (2020) Advanced vehicle dynamics through active aerodynamics and active body control. In: International design engineering technical conferences and computers and information in engineering conference, vol 83938, p V004T04A011. American Society of Mechanical Engineers
14. Sellitto A, Riccio A (2019) Overview and future advanced engineering applications for morphing surfaces by shape memory alloy materials. Materials 12(5):708
15. Shreekrishna S, Nachimuthu R, Nair VS (2023) A review on shape memory alloys and their prominence in automotive technology. J Intell Mater Syst Struct 34(5):499–524
16. Sleight M, Peltier L, Piotrowski B, Meraghni F (2022) Design, characterization, and finite-element optimization of a two-way assisted through superelasticity torsion actuator. Shape Memory Superelasticity 8(4):295–307
17. Bogue R (2014) Smart materials: a review of capabilities and applications. Assem Autom 34(1):16–22
18. Battaglia M, Sellitto A, Giamundo A, Visone M, Riccio A (2023) Shape memory alloys applied to automotive adaptive aerodynamics. Materials 16(13):4832
19. Costanza G, Tata ME (2020) Shape memory alloys for aerospace, recent developments, and new applications: a short review. Materials 13(8):1856
20. Bettini P, Rigamonti D, Sala G (2021). SMA for composite aerospace structures. In: Shape memory alloy engineering, pp 561–590. Butterworth-Heinemann
21. Kim H, Ahn SK, Mackie DM, Kwon J, Kim SH, Choi C et al (2020) Shape morphing smart 3D actuator materials for micro soft robot. Mater Today 41:243–269
22. Ruth DJS, Sohn JW, Dhanalakshmi K, Choi SB (2022) Control aspects of shape memory alloys in robotics applications: a review over the last decade. Sensors 22(13):4860
23. Dawood NM, Ali ARKA, Atiyah AA (2019) Fabrication of porous NiTi shape memory alloy objects by powder metallurgy for biomedical applications. In: IOP Conference Series: Materials Science and Engineering, Vol. 518, No. 3, p 032056). IOP Publishing
24. Nair VS, Nachimuthu R (2022) The role of NiTi shape memory alloys in quality of life improvement through medical advancements: a comprehensive review. Proc Inst Mech Eng H 236(7):923–950
25. Jani JM, Leary M, Subic A, Gibson MA (2014) A review of shape memory alloy research, applications and opportunities. Mater Des 1980–2015(56):1078–1113
26. Firstov GS, Van Humbeeck J, Koval YN (2004) High-temperature shape memory alloys: some recent developments. Mater Sci Eng A 378(1–2):2–10
27. Van Humbeeck J (2012) Shape memory alloys with high transformation temperatures. Mater Res Bull 47(10):2966–2968
28. Brinson LC (1993) One-dimensional constitutive behavior of shape memory alloys: Thermomechanical derivation with non-constant material functions and redefined martensite internal variable. J Intell Mater Syst Struct 4:229–242
29. Eggeler G, Hornbogen E, Yawny A, Heckmann A, Wagner M (2004) Structural and functional fatigue of NiTi shape memory alloys. Mater Sci Eng A 378(1–2):24–33
30. Chemisky Y, Hartl DJ, Meraghni F (2018) Three-dimensional constitutive model for structural and functional fatigue of shape memory alloy actuators. Int J Fatigue 112:263–278
31. Riccio A, Saputo S, Sellitto A (2022) Attuatore Bistabile. UiBM Patent 102020000025483
32. Riccio A, Napolitano C, Sellitto A, Acanfora V, Zarrelli M (2021) Development of a combined micro-macro mechanics analytical approach to design shape memory alloy spring-based actuators and its experimental validation. Sensors 21(16):5506
33. Riccio A, Saputo S, Zarrelli M, Sellitto A, Napolitano C, Acanfora V (2021) Shape memory alloy-based actuator: experimental and modelling. In: 2021 IEEE 8th international workshop on metrology for aerospace (MetroAeroSpace), pp 665–671. IEEE